Gate fidelity and coherence of an electron spin in an Si/SiGe quantum dot with micromagnet

Erika Kawakami[a,b], Thibaut Jullien[a,b,1], Pasquale Scarlino[a,b], Daniel R. Ward[c], Donald E. Savage[c], Max G. Lagally[c], Viatcheslav V. Dobrovitski[d], Mark Friesen[c], Susan N. Coppersmith[c,2], Mark A. Eriksson[c], and Lieven M. K. Vandersypen[a,b,e,2]

[a]QuTech, 2628 CJ Delft, The Netherlands; [b]Kavli Institute of Nanoscience, Delft University of Technology, 2628 CJ Delft, The Netherlands; [c]University of Wisconsin-Madison, Madison, WI 53706; [d]Ames Laboratory, US Department of Energy, Iowa State University, Ames, IA 50011; and [e]Components Research, Intel Corporation, Hillsboro, OR 97124

Contributed by Susan N. Coppersmith, August 28, 2016 (sent for review March 1, 2016; reviewed by Guido Burkard and John J. L. Morton)

The gate fidelity and the coherence time of a quantum bit (qubit) are important benchmarks for quantum computation. We construct a qubit using a single electron spin in an Si/SiGe quantum dot and control it electrically via an artificial spin-orbit field from a micromagnet. We measure an average single-qubit gate fidelity of ∼99% using randomized benchmarking, which is consistent with dephasing from the slowly evolving nuclear spins in the substrate. The coherence time measured using dynamical decoupling extends up to ∼400 μs for 128 decoupling pulses, with no sign of saturation. We find evidence that the coherence time is limited by noise in the 10-kHz to 1-MHz range, possibly because charge noise affects the spin via the micromagnet gradient. This work shows that an electron spin in an Si/SiGe quantum dot is a good candidate for quantum information processing as well as for a quantum memory, even without isotopic purification.

Si/SiGe quantum dot | qubit | dynamical decoupling | randomized benchmarking | electron spin

The performance of a quantum bit (qubit) is characterized by how accurately operations on the qubit are implemented and for how long its state is preserved. For improving qubit performance, it is important to identify the nature of the noise that introduces gate errors and leads to loss of qubit coherence. Ultimately, what counts is to balance the ability to drive fast qubit operations and the need for long coherence times (1).

Electron spins in Si quantum dots are now known to be one of the most promising qubit realizations for their potential to scale up and their long coherence times (2–10). Using magnetic resonance on an electron spin bound to a phosphorus impurity in isotopically purified ^{28}Si (5) or confined in a ^{28}Si metal–oxide–semiconductor (MOS) quantum dot (3), ∼0.3-MHz Rabi frequencies, gate fidelities over 99.5%, and spin memory times of tens to hundreds of milliseconds have been achieved. Also, electrical control of an electron spin has been demonstrated in a (natural abundance) Si/SiGe quantum dot, which was achieved by applying an AC electric field that oscillates the electron wave function back and forth in the gradient magnetic field of a local micromagnet (7). The advantage of electrical control over magnetic control is that electric fields can be generated without the need for microwave cavities or striplines and allows better spatial selectivity, which simplifies individual addressing of qubits. However, the magnetic field gradient also makes the qubit sensitive to electrical noise, so it is important to examine whether the field gradient limits the spin coherence time and the gate fidelity.

In our previous work (7), the effect of electrical noise on spin coherence and gate fidelity was overwhelmed by transitions between the lowest two valley-orbit states. Because different valley-orbit states have slightly different Larmor frequencies, such a transition will quickly randomize the phase of the electron spin. If valley-orbit transitions can be (largely) avoided, then the question becomes what limits coherence and fidelities instead.

Here we measure the gate fidelity and spin echo times for an electron spin in an Si/SiGe quantum dot in a regime where the electron stably remains in the lowest valley-orbit state for long times, and where the corresponding resonance condition is well separated from that associated with the other valley-orbit state. To learn more about the dominant noise sources in this new regime, we use dynamical decoupling experiments to extract the noise spectrum in the range of 5 kHz to 1 MHz, and we compare this spectrum with spectra derived from numerical simulations for various noise sources. We also study the influence of the various noise sources on the gate fidelity.

Device and Measurement Setup

A single electron spin is confined in a gate-defined quantum dot in an undoped Si/SiGe heterostructure (6–8) (Fig. 1). The sample is attached to the mixing chamber (MC) stage of a dilution refrigerator with base temperature of ∼25 mK, and subject to a static external magnetic field of 794.4 mT along the direction as indicated in Fig. 1, *Inset*. Spin rotations are achieved by applying microwave excitation to one of the gates, which oscillates the electron wave function back and forth in the magnetic field gradient produced by two cobalt micromagnets fabricated on top of the device. The device used in this work is the same as in the

Significance

A quantum computer is able to solve certain problems that cannot be solved by a classical computer within a reasonable time. The building block of a quantum computer is called a quantum bit (qubit), the counterpart of the conventional binary digit (bit). A qubit unavoidably interacts with its environment, leading to errors in the qubit state. This article reports on the qubit performance of an electron spin in a silicon/silicon-germanium (Si/SiGe) quantum dot, and examines the dominant error mechanisms. We demonstrate that this qubit can be electrically controlled with sufficient accuracy so that remaining errors could, in principle, be corrected using known protocols, even without isotopically purified silicon. This qubit also offers a quantum memory that lasts for almost 0.5 ms.

Author contributions: E.K., T.J., P.S., M.F., S.N.C., M.A.E., and L.M.K.V. designed research; E.K., T.J., P.S., D.R.W., D.E.S., M.G.L., V.V.D., M.F., S.N.C., M.A.E., and L.M.K.V. performed research; E.K., T.J., P.S., V.V.D., M.F., S.N.C., M.A.E., and L.M.K.V. analyzed data; and E.K., P.S., V.V.D., M.F., S.N.C., M.A.E., and L.M.K.V. wrote the paper.

Reviewers: G.B., University of Konstanz; and J.J.L.M., University College London.

The authors declare no conflict of interest.

Freely available online through the PNAS open access option.

[1]Deceased February 27, 2015.

[2]To whom correspondence may be addressed. Email: snc@physics.wisc.edu or l.m.k.vandersypen@tudelft.nl.

This article contains supporting information online at www.pnas.org/lookup/suppl/doi:10.1073/pnas.1603251113/-/DCSupplemental.

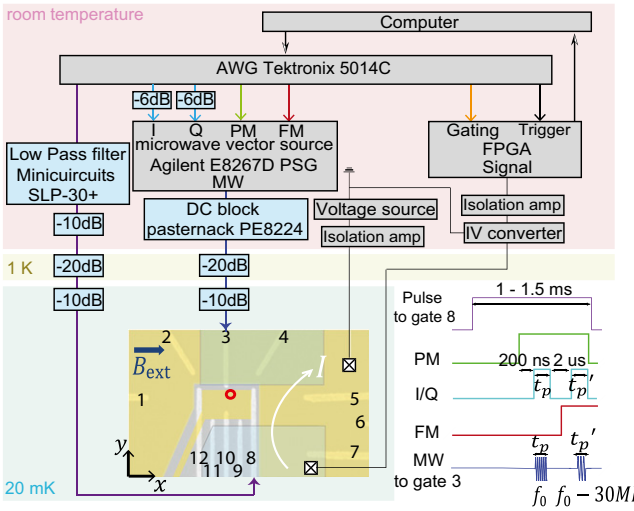

Fig. 1. Device schematic and block diagram depicting the generation of gate voltage pulses and phase-controlled microwave bursts, and readout trace analysis and postanalysis using an FPGA. The false-color device image shows (in the lower left at 20 mK) a fabricated pattern of split gates, labeled 1 to 12. For this experiment, we create a single quantum dot (estimated location indicated by a red circle) and a sensing dot. The spin state of the electron is read out by monitoring the level of the sensing current *I*. Green semitransparent rectangles show the position of two 200-nm-thick Co micromagnets. The yellow-shaded areas show the location of two accumulation gates, one for the reservoirs and another for the double quantum dot region. The main components of the block diagram are described in *Device and Measurement Setup*. For the I/Q inputs, 6-dB attenuators are added to reduce the noise from the AWG. To reduce the noise going to the sample from the AWG, a Minicircuit low-pass filter SLP-30+ and a 10-dB attenuator are added at room temperature. A Pasternack DC block PE8224 is added at room temperature behind the microwave source to reduce low-frequency noise. The 30-dB attenuation at low temperature is divided over a 20-dB attenuator at the 1-K plate and a 10-dB attenuator at the MC stage for each of two high-frequency lines, connected to gate 3 and gate 8. One of the two ohmic contacts of the sensing dot is connected to a room-temperature voltage source, and the other is connected to the input of a homemade junction gate field-effect transistor (JFET) current-to-voltage (IV) converter via resistor–capacitor (RC) and copper powder filters mounted at the MC stage and capacitor-input filters (pi filters) at room temperature. The output voltage signal of the IV converter is digitized and processed by an FPGA. A gating pulse sent to the FPGA defines the segment of the signal that is to be analyzed. An additional trigger pulse is applied to the FPGA before the entire sequence starts. (*Inset*) The voltage pulse applied to gate 8 (purple line), the pulses used for PM (green line), gating the FPGA (orange line), I/Q modulation (light blue line), and FM (red line), and the microwave burst applied to gate 3 (blue line) during the manipulation stage.

previous work (7), but the applied gate voltages are set differently to obtain a higher valley-orbit splitting.

The measurement scheme consists of four stages: initialization, manipulation, readout, and emptying, as shown in ref. 7. Differently from ref. 7, the four-stage voltage pulse is applied to gate 8, and the microwave excitation is applied to gate 3. The initialization and readout stages take 4 ms to 5 ms, and the manipulation and emptying stages last 1 ms to 1.5 ms.

Because the experimental details of the setup are important for the results shown in this paper, we here summarize the key components. A voltage pulse applied to gate 8 is generated by an arbitrary waveform generator (Tektronix AWG 5014C). Phase-controlled microwave bursts are generated by an Agilent microwave vector source E8267D with the I (in-phase) and Q (out-of-phase) components controlled by two channels of the AWG. The on/off ratio of the I/Q modulation is 40 dB. If the microwave power arriving at the sample is not sufficiently suppressed in the "off" state, the control fidelity is reduced and the effective electron temperature increases, which, in turn, will result in lower readout and initialization fidelities. Reduced fidelities were indeed observed when applying high-power microwave excitation (>15 dBm at the source) using I/Q modulation only. As a solution, we use digital pulse modulation (PM) in series with the I/Q modulation, which gives a total on/off ratio of ∼120 dB. A drawback of PM is that the switching rate is lower. Therefore, the PM is turned on 200 ns before the I/Q modulation is turned on (Fig. 1, *Inset*). We also observe that the total microwave burst time applied to the sample per cycle affects the readout and initialization fidelities (*SI Appendix*). To keep the readout and initialization fidelities constant, we apply an off-resonance microwave burst (with microwave frequency detuned by 30 MHz from the resonance frequency) 2 μs after the on-resonance microwave burst, so that the combined duration of the two bursts is fixed. To achieve this rapid shift of the microwave frequency, we used frequency modulation (FM) controlled by another channel of the AWG. FM is turned on 1 μs after the on-resonance burst is turned off (Fig. 1, *Inset*).

The electron spin state is read out via spin-to-charge conversion by aligning the Fermi level of the reservoir between the spin-down and spin-up states and below the spin-up state combined with real-time charge detection (11). The probability that the current exceeds a predefined threshold during the readout stage is interpreted as the spin-up probability of the electron (7). The analysis of the real-time traces and the statistical analysis of the readout events are done on the fly using a field-programmable gate array (FPGA) as depicted in Fig. 1; this allows us to measure faster without waiting for the transfer of real-time traces to a computer. Data points were taken by cycling through the various burst times, spin echo waiting times, or randomized gate sequences, and repeating these entire cycles 250 to 1,000 times. This order of the measurements helps to suppress artifacts in the data caused by slow drift in the setup or sample.

High-Quality Rabi Oscillations

Rabi oscillations are recorded by varying the burst time and the microwave frequency. With the present gate voltage settings, the spin resonance frequencies corresponding to the two lowest valley-orbit states are separated by ∼5 MHz (at $B_{ext} = 794.4$ mT), so that two well-separated chevron patterns characteristic for Rabi oscillations are observed (Fig. 2*A*). This difference of ∼5 MHz results mainly from slightly different electron *g* factors

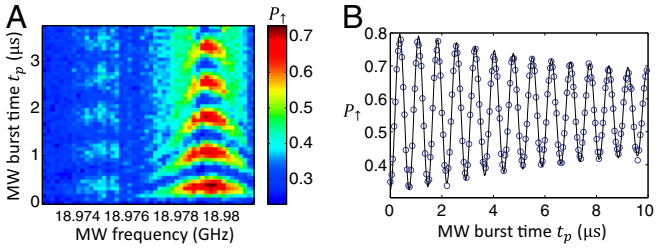

Fig. 2. (*A*) Measured spin-up probability, $P_\uparrow$, as a function of f_{MW} and burst time t_p [microwave (MW) power at the source $P = 18.85$ dBm], showing two Rabi chevron patterns corresponding to the two valley-orbit states. The resonance frequency of the valley-orbit ground state is 18.9795 GHz, and that of the excited state is 18.9750 GHz. The signal coming from the excited state is much smaller due to its lower population. (*B*) Measured spin-up probability, $P_\uparrow$, showing a Rabi oscillation for the ground valley-orbit state (blue circles). During the manipulation stage, on-resonance microwave excitation (at $f_{MW} = 18.9795$ GHz) was applied for a time t_p, and off-resonance microwave ($f_{MW} = 18.9195$ GHz) was applied for a time $t_p' = 10\ \mu s - t_p$, to keep the total duration of the microwave bursts fixed to 10 μs for every data point. The black line shows a numerical fit with a model that includes a constant driving field in the rotating frame (which is a fit parameter) and (quasi-)static noise modeled by a Gaussian distribution of resonance offsets with width 0.63 MHz (FWHM).

between the two valley-orbit states. The population of the valley-orbit ground state is estimated to be ~80% from Fig. 2*A*, which is higher than in our previous work (7), and implies a higher valley-orbit splitting. (Due to many unknown parameters, it is difficult to obtain a reliable estimate of the valley-orbit splitting. Nevertheless, assuming that the values of these parameters are equal between the previous work (7) and this work, the higher population of the ground valley-orbit state implies a higher valley-orbit splitting. See *SI Appendix* for more details.) Fig. 2*B* shows a Rabi oscillation of a single spin with the electron in the ground valley-orbit state. The Rabi frequency extracted from the data is 1.345 MHz. The decay of the oscillation is what we would expect assuming a statistical distribution of resonance conditions with a line width of 0.63 MHz (FWHM), which is the number extracted from the continuous wave response (7). This line width corresponds to $T_2^* \approx 1$ μs, and is presumably dominated by the 4.7% ^{29}Si spins in the substrate, similar to ref. 7. Here there is no evidence of additional decay mechanisms. In particular, we do not see any indication of intervalley switching with or without spin flip, or the combined effects of electrical noise and the magnetic field gradient.

Dynamical Decoupling

Next we examine the spin memory time of this electrically controlled spin qubit. In our previous work (7, 12), due to switching between the two valley-orbit states, the Hahn echo decay was exponential with coherence time of ~40 μs. Furthermore, we were unable to extend the coherence time using multiple echo pulses. Due to the difference in Larmor frequency between two valley-orbit states, as soon as a switch from one to the other valley-orbit state occurred, phase information could not be recovered by echo pulses. In this work, we observe significantly extended coherence times, presumably because the switching between valleys is slower in the present gate voltage configuration.

We study the spin memory characteristics using two types of two-axis dynamical decoupling sequences, based on the XY4 (13), $(XY4)^n$ [sometimes called vCDD (14)], and XY8 (15) protocols. Fig. 3 *A* and *B*, *Insets* show the $(XY4)^n$ and XY8 pulse sequences for 16 π pulses. We use X and Y to denote π rotations about $\hat{x}$ and $\hat{y}$, and we use $\bar{X}$ and $\bar{Y}$ for rotations about $-\hat{x}$ and $-\hat{y}$. Such two-axis decoupling sequences are chosen to reduce the effect of pulse imperfections and to equally preserve the spin components along all directions in the $\hat{x}-\hat{y}$ plane (16), which is important for quantum information processing. One-axis decoupling sequences such as Car–Purcell–Meiboom–Gill (CPMG) (17, 18) may artificially preserve a specific spin component for a longer time than two-axis decoupling sequences, but with a reduced coherence time of the orthogonal spin component (19–21). The visibility of the echo amplitude decreases for larger numbers of π pulses, N_π, due to the pulse imperfections. Therefore, to facilitate direct comparison of the decay rates with different numbers of π pulses, in Fig. 3 *A* and *B*, we show the data, normalized to the echo amplitude at $t_{\text{wait}} = 0$, as a function of the total wait time t_{wait} for $(XY4)^n$ and XY8, respectively.

To analyze these decay curves, we adopt a semiclassical approach, in which the decay curve of the echo amplitude is written as

$$P(t_{\text{wait}}) = \exp[-W(t_{\text{wait}})] \quad [1]$$

with

$$W(t_{\text{wait}}) = \int_{-\infty}^{\infty} \frac{S(\omega)}{2\pi} \frac{F(\omega)}{\omega^2} d\omega. \quad [2]$$

$S(\omega)$ is the noise spectrum that produces an effective magnetic field fluctuation $\delta b(t)$ along the same direction as the quantization axis (22). More concretely, the relation between $S(\omega)$ and

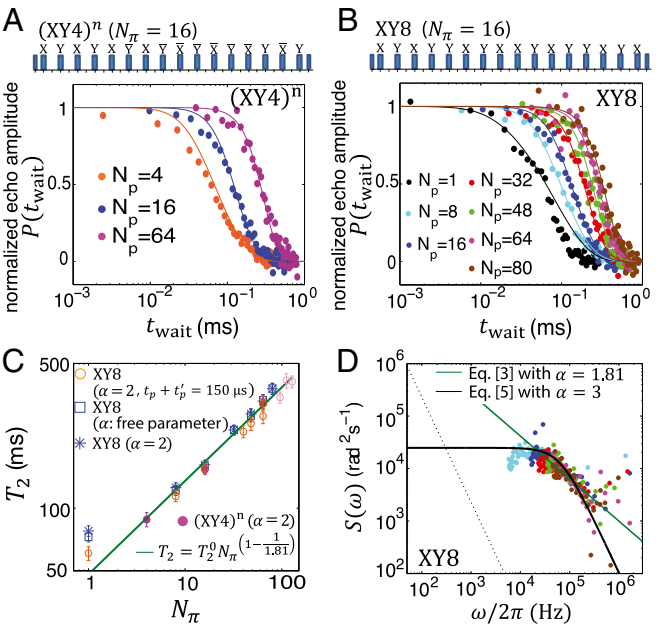

Fig. 3. (*A*) Normalized spin echo amplitude as a function of the total waiting time t_{wait} using the $(XY4)^n$ pulse sequence for $N_\pi = 4$ (orange points), 16 (blue points), and 64 (purple points) pulses (concatenated level $n =$ 1, 2, and 3, respectively). (*Inset*) The $(XY4)^n$ pulse sequence for $N_\pi = 16$ ($n = 2$). The first and the last pulses are $\pi/2$ pulses, and the 16 pulses in the middle are π pulses. X, $\bar{X}$, $\bar{Y}$, or Y indicate the phase of the pulses. The solid lines present fits using Eq. **1** with Eqs. **2** and **5** for $\alpha = 3$. (*B*) Similar to *A* but using a Hahn echo sequence for $N_\pi = 1$ and an XY8 sequence for $N_\pi = 8,16,32,48,64,80$. (*Inset*) XY8 pulse sequence for $N_\pi = 16$. Fits are as in *A*, except that the solid line for $N_\pi = 1$ is the decay curve with *A* and τ_c obtained from the fit to the other six decay curves in *B*. (*C*) Coherence time, T_2, as a function of the number of π pulses N_π using XY8 (blue asterisks, blue squares, and orange circles) and $(XY4)^n$ (purple circles). See *SI Appendix* for the pulse sequences used for pink open circles. The T_2 values are obtained by fitting Eq. **4** to the decay curves. The choice of α did not much affect the extracted T_2. The values shown are for $\alpha = 2$ except for the blue squares, for which α is left as a fitting parameter. The green line presents a fit to the data (leaving out $N_\pi = 1$) using $T_2 = T_2^0 N_\pi^{(1-1/\alpha)}$. From this fit, we obtained $T_2^0 = 48 \pm 8$ μs and $\alpha = 1.81 \pm 0.14$. (*D*) Noise spectrum extracted from *B*. The green solid line corresponds to Eq. **3** with $T_2^0 = 48$ μs and $\alpha = 1.81$. The black line presents a fit using Eq. **5**; see text. The dotted black line represents the calculated noise spectrum produced by the ^{29}Si nuclear spin dynamics (see *SI Appendix* for the details of the calculation).

$\delta b(t)$ is described as $S(\omega) = \int_{-\infty}^{\infty} \gamma_e^2 \langle \delta b(0) \delta b(t) \rangle e^{i\omega t} dt$ with γ_e as the gyromagnetic ratio of the electron. $F(\omega)$ is the filter function of the pulse sequence (23, 24). First, we assume that the noise spectrum dominating the decoherence is described by a power law,

$$S(\omega) = \frac{K}{\omega^{\alpha-1}}, \quad [3]$$

as seen in GaAs quantum dots (25) and NV centers in diamond (16). Under this assumption, if the filter function $F(\omega)$ is sufficiently narrow around $\omega = \pi N_\pi / t_{\text{wait}}$ (which we verified is the case for $N_\pi \geq 4$), the decay curve can be written as (26)

$$P(t_{\text{wait}}) = \exp\left[-\left(\frac{t_{\text{wait}}}{T_2}\right)^\alpha\right], \quad [4]$$

with $T_2 = T_2^0 N_\pi^{[1-(1/\alpha)]}$ and $T_2^0 = (2/K)^{(1/\alpha)} \pi^{1-(1/\alpha)}$. Fig. 3*C* shows T_2 as a function of the number of π pulses obtained by fitting Eq. **4** to the decay curves. The longest T_2 time reached is ~400 μs with XY8 and $N_\pi = 128$ (data shown in *SI Appendix*). We fitted

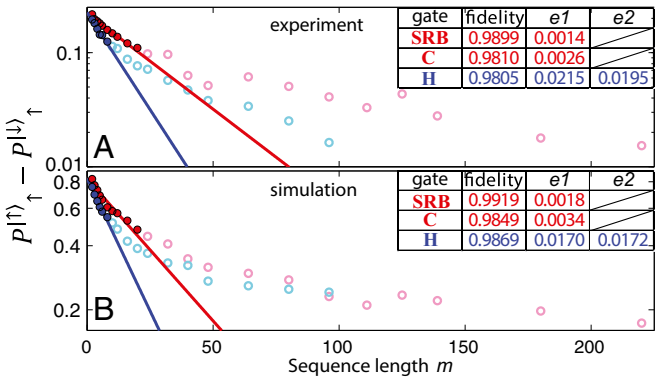

Fig. 4. Randomized benchmarking. The difference between the spin-up probability with spin-up as the target state and with spin-down as the target state, $P^{|\uparrow\rangle}_{\uparrow} - P^{|\downarrow\rangle}_{\uparrow}$, is plotted as a function of the number of Clifford gates, m. The SRB curve (red circles) is measured after applying randomized sequences of m Clifford gates and a final Clifford gate C_{m+1}. The IRB curve is measured by interleaving the Hadamard gate with the same random sequence of Clifford gates (blue circles). (*A*) The experimental results. (*B*) The results of numerical simulations (see *Randomized Benchmarking*). The experiments and simulations use the same 119 random sequences from $m = 2$ to 220. Each experimental data point is the average of 250 single-shot cycles. For the numerical simulation, we averaged over 1,000 repetitions, and, for each repetition, we sample δb_0 and include a different time-domain realization of $\delta b'(t)$. In the simulation, the readout and initialization fidelities are assumed to be perfect. The π rotation time is 366 ns for the experiments and 360 ns for the simulation. The delay time between pulses is set to be 5 ns for both the measurements and the simulations. The red and blue curves present fits of the form Ap^m to the data with $t_p < 8$ μs. (*Insets*) The gate fidelities extracted from the fits. The first row (SRB) and the second row (C) show the average fidelity per single gate and per Clifford gate, respectively, obtained from the SRB measurements. The third row (H) shows the fidelity of the Hadamard gate obtained from IRB; *e*1 and *e*2 are as defined in Table 1.

$T_2 = T_2^0 N_\pi^{[1-(1/\alpha)]}$ to the data (leaving out the case $N_\pi = 1$, the Hahn echo), and the resulting fit is shown in green in Fig. 3*C*.

We can derive the noise spectrum from the decay curves in Fig. 3 *A* and *B* using the fact that the filter function is narrow around $\omega = \pi N_\pi / t_{\text{wait}}$ for $N_\pi \geq 4$ (22) (*SI Appendix*). The circles in Fig. 3*D* show the noise spectrum extracted from six decay curves in Fig. 3*B*. The colors of the circles in Fig. 3*D* correspond to the colors used in Fig. 3*B* for different N_π. The green solid line in Fig. 3*D* is based on Eq. **3**, with T_2^0 and α obtained from the fit (green line) to the data in Fig. 3*C*; its decay is close to a $1/f$ decay. Although this line shows an overall good agreement with the noise spectrum extracted from the decay curves, it does not match with the flat region at $\omega/2\pi \lesssim 30$ kHz.

To capture both the flat and decaying parts of the spectrum and obtain more insight into the nature of the noise spectrum, we now write the noise spectrum in the form

$$S(\omega) = \frac{A}{1 + (\omega\tau_c)^{\alpha-1}}, \qquad [5]$$

where τ_c is the correlation time of the fluctuations in the environment that dominate the dynamical decoupling decay. We fit Eq. **1** to the six decay curves (leaving out $N_\pi = 1$) in Fig. 3*B* simultaneously, using also Eqs. **2** and **5**, with A and τ_c as the only fitting parameters. We first perform this fit (numerically) using $\alpha = 2$, close to the previously fitted value $\alpha = 1.8$ obtained using Eq. **3**, but the fits deviate from the measured echo decays (see *SI Appendix*, Fig. S5*E*). A better fit to the echo decay data using Eq. **5** is obtained for $\alpha = 3$ (Fig. 3*B*), in which case Eq. **2** can be expressed analytically (20). The fits in Fig. 3*B* yield $A = (2.5 \pm 0.2) \cdot 10^4$ rad^2·s^{-1} and $\tau_c = 2.46 \pm 0.17$ μs. The resulting fit, plotted as a thick black line in Fig. 3*D*, shows reasonable agreement with $S(\omega)$ obtained from the experimental data.

Extrapolating the fitted noise spectrum to frequencies below 5 kHz, where we do not have experimental data, the noise spectral density looks flat; this would result in an exponential Ramsey decay with $T_2^* \approx 80$ μs (22). However, the measured Ramsey decay is Gaussian and has a much shorter $T_2^* \approx 1$ μs. Therefore, the noise power at low frequencies must exceed the solid horizontal black line in Fig. 3*D* (*SI Appendix*).

We now turn to the noise mechanisms and examine whether the hyperfine coupling of the electron spin with the evolving nuclear spins can explain the observed noise spectrum. Nuclear spin dynamics have two main mechanisms, hyperfine-mediated and dipole–dipole interactions between nuclear spins. Decoherence due to the hyperfine-mediated interactions is negligible in Si at $B \approx 800$ mT (27) (*SI Appendix*). However, magnetic dipole–dipole induced nuclear spin dynamics cannot be neglected. We performed numerical simulations of the spectrum of the nuclear spin noise and of the Hahn echo decay for a dot with 4.7% of ^{29}Si nuclei (natural abundance) within the coupled pair-cluster expansion (28) for several choices of the quantum dot parameters. A calculated spectrum is approximated to an analytical expression: $2\sigma_\omega^2 \tau_n / [1 + (\omega\tau_n)^2]$ with the correlation time of the nuclear spin bath $\tau_n \approx 10^4$ ms and the amplitude $\sigma_\omega \approx 10^6$ rad/s is shown by the dotted line in Fig. 3*D*. The measured Gaussian-shape Ramsey decay with $T_2^* \approx 1$ μs is consistent with this spectrum, so, presumably, the randomly oriented ^{29}Si nuclear spins dominate the noise at low frequencies (7, 22) (see *SI Appendix* for details); they also dominate the gate fidelities discussed in *Randomized Benchmarking*. However, at higher frequencies, even though the noise spectrum calculated from the nuclear spin dynamics has the same shape as Eq. **5** with $\alpha = 3$, the amplitude and the correlation time are significantly different from the noise spectrum measured by the dynamical decoupling. With the calculated correlation time and the amplitude for the nuclear spins, the Hahn echo decay time T_2 would be above 0.5 ms, which is much longer than the measured value of 70 μs. Nuclear spin noise thus cannot explain the observed Hahn echo decay.

We therefore conclude that the noise spectrum consists of at least two contributions: nuclear spin noise at low frequencies and another mechanism at higher frequencies. At higher frequencies, the noise spectrum decays as $1/f^2$ taking $\alpha = 3$, but we see that a $\approx 1/f$ decay (green line) also fits the frequency dependence of the data points well. It is possible that this part of the spectrum is dominated by charge noise, which couples to the spin due to the magnetic field gradient from the micromagnets. Thus, charge noise may effectively induce magnetic $1/f$ or $1/f^2$ noise. To give a feeling for numbers, a two-level magnetic field fluctuation of ±0.4 μT, which, given the micromagnet gradient, corresponds to a ~4 pm shift back and forth in the dot position, gives a Lorentzian

Table 1. Measured gate fidelities for five representative gates, extracted using IRB

Gate	Fidelity	*e*1	*e*2
T ($\pi/4$ rotation around $\hat{z}$)	0.9891	0.0282	0.0272
H (π rotation around $\hat{x} + \hat{z}/2$)	0.9805	0.0215	0.0195
x ($\pi/2$ rotation around $\hat{x}$)	0.9893	0.0285	0.0368
z ($\pi/2$ rotation around $\hat{z}$)	0.9813	0.0198	0.0231
X (π rotation around $\hat{x}$)	0.9842	0.0622	0.0325
Z (π rotation around $\hat{z}$)	0.9917	0.0670	0.0401

Here, *e*1 and *e*2 are errors in the fidelities; *e*1 is calculated from the 95% confidence interval on the fit coefficient p, and *e*2 is an upper bound arising from imperfect random gates, calculated according to the formulas in ref. 31. As the T gate is not a Clifford gate, we interleaved two successive T gates, following ref. 32.

noise spectrum that matches the solid line in Fig. 3*D* [Eq. **5** with $\alpha = 3$, $A = (2.5 \pm 0.2) \cdot 10^4$ rad^2·s^{-1}, and $\tau_c = 2.46 \pm 0.17$ μs] (29).

Randomized Benchmarking

We measured the average gate fidelity using standard randomized benchmarking (SRB), which is known as an efficient way to measure the gate fidelity without suffering from initialization and readout errors (30, 31). The specific procedure is as follows. After initializing the electron to the spin-down state, we apply randomized sequences of m Clifford gates and a final Clifford gate C_{m+1} that is chosen so that the final target state in the absence of errors is either spin-up or spin-down. Every Clifford gate is implemented by composing π and $\pi/2$ rotations around two axes, following ref. 32. Applying randomized sequences of imperfect Clifford gates acts as a depolarizing channel (30, 31). The depolarization parameter p reflects the imperfection of the average of 24 Clifford gates. Under certain assumptions, for m successive Clifford gates, the depolarization parameter is p^m.

We measure the spin-up probability both for the case where spin-up is the target state, $P_\uparrow^{|\uparrow\rangle}$, and for the case where spin-down is the target state, $P_\uparrow^{|\downarrow\rangle}$, for 119 different randomized sequences for each choice of m, and varying m from 2 to 220. The difference of the measured spin-up probability for these two cases, $P_\uparrow^{|\uparrow\rangle} - P_\uparrow^{|\downarrow\rangle}$, is plotted with red circles in Fig. 4*A*. Theoretically, $P_\uparrow^{|\uparrow\rangle} - P_\uparrow^{|\downarrow\rangle}$ is expressed as (3, 33)

$$P_\uparrow^{|\uparrow\rangle} - P_\uparrow^{|\downarrow\rangle} = ap^m, \quad [6]$$

where a is a prefactor that does not depend on the gate error. As seen in Eq. **6**, differently from quantum process tomography (6, 34, 35), the measurement of the gate fidelity is not affected by the initialization and readout infidelities, assuming these infidelities are constant throughout the measurement. To keep the readout and initialization fidelities constant for different m, we kept the total microwave burst time $t_p + t_p' = 150$ μs. Due to the longer total microwave burst time, the readout and initialization infidelities are higher than in Fig. 2. This is the reason that, initially, $P_\uparrow^{|\uparrow\rangle} - P_\uparrow^{|\downarrow\rangle}$ is 20% instead of 45%.

Fig. 4*A* shows that the measured decay does not follow a simple exponential p^m. This behavior is reproduced by numerical simulations of the randomized benchmarking experiment, using the same set of randomized sequences as used in the experiments and assuming that the magnetic field fluctuations are characterized by $\delta b(t)$, the combination of the high-frequency noise $\delta b'(t)$ and the (quasi-)static noise δb_0,

$$\delta b(t) = \delta b_0 + \delta b'(t), \quad [7]$$

where δb_0 again has a Gaussian distribution with FWHM of 0.63 MHz, and $\delta b'(t)$ is expressed by Eq. **5** using $\alpha = 3$, $A = 2.5 \cdot 10^4$ rad^2·s^{-1}, and $\tau_c = 2.46$ μs. The simulation results are shown in Fig. 4*B* and show good agreement with experiment.

To evaluate explicitly the relative contribution of δb_0 and $\delta b'(t)$ to the randomized benchmarking decay, we repeated the numerical simulation including, at first, only the high-frequency noise $\delta b'(t)$, in which case the decay is extremely slow. Next, we include only the (quasi-)static noise δb_0 and find almost exactly the same decay as with the combination of the two noise contributions. This indicates that the (quasi-)static noise is mainly responsible for the gate error, whereas the contribution from the high-frequency noise is small (*SI Appendix*). This dominant contribution of the (quasi-)static noise to the gate error is consistent with an earlier report (36), in which it was also shown that ensemble averaging over individual exponential decays can lead to a nonexponential decay. Repeated measurements in the presence of low-frequency noise effectively lead to such ensemble averaging.

Because the measured SRB decay is not of the form ap^m, we should be cautious using the fidelity numbers extracted from this procedure (37). We see that, both in experiment and simulation, the decay begins to deviate from a single exponential (straight line in the semilog plot) for on-resonance microwave bursts with $t_p \gtrsim 8$ μs. These are the data points with open circles in Fig. 4. We fitted to the decay curves for $t_p < 8$ μs to ap^m and obtained $p = 0.9620 \pm 0.0051$; from this, the average fidelity of a Clifford gate is $1 - (1-p)/2 = 98.10 \pm 0.26\%$, and the average fidelity for a single π or $\pi/2$ rotation around $\hat{x}$ or $\hat{y}$ is calculated to be $1 - (1-p)/2/1.875 = 98.99 \pm 0.14\%$.

We also characterized the fidelity of individual gates using interleaved randomized benchmarking (IRB). In this procedure, a specific gate is interleaved between randomized Clifford gates. The depolarizing parameter now becomes bigger than in SRB, due to the imperfections of the interleaved gate. From the difference in the depolarizing parameter between SRB and IRB, the fidelity of the interleaved gate is extracted. In Fig. 4*A*, the blue circles show the case where the Hadamard gate is the interleaved gate. The Hadamard gate is implemented by a π rotation around the $\hat{x}$ axis and a $\pi/2$ rotation around the $-\hat{y}$ axis. By fitting $a_H p_H^m$ to the decay curve (again for $t_p < 8$ μs), $p_H = 0.9245 \pm 0.0197$ is obtained. The fidelity of the Hadamard gate is calculated to be $1 - (1 - p_H/p)/2 = 98.05 \pm 2.15\%$. In the same way, we measured the fidelities for several other common gates (Table 1). Although, also for IRB, the decay is not exponential, the gate fidelities extracted from IRB for the first 8 μs appear roughly consistent with the fidelities extracted from SRB.

Discussion and Conclusion

We have shown that the average single gate fidelity for a single electron spin confined in a ^{nat}Si/SiGe quantum dot approaches the fault-tolerance threshold for surface codes (1). The low-frequency noise that limits gate fidelity is well explained by the nuclear spin randomness given the natural abundance of ^{29}Si. Therefore, we can increase gate fidelities by reducing the abundance of ^{29}Si using isotopically enriched ^{28}Si (3, 5) or by using composite pulses (38). Also, the readout fidelity can be boosted to the fault-tolerance threshold by using Pauli spin blockade readout (39) and RF reflectometry (40). The longest coherence time measured using dynamical decoupling is ∼400 μs. We revealed that the noise level is flat in the range of 5 kHz to 30 kHz and decreases with frequency in the range of 30 kHz to 1 MHz. In this frequency range (5 kHz to 1 MHz), the measured noise level is higher than expected from the dynamics of the ^{29}Si nuclear spins. Instead, charge noise in combination with a local magnetic field gradient may be responsible. If charge noise is dominant, dynamical decoupling decay times can be further extended by positioning the electron spin so that the gradient of the longitudinal component of the magnetic field gradient vanishes, while keeping the transverse component nonzero as needed for driving spin rotations. At that point, we can reap the full benefits from moving to ^{28}Si enriched material for maximal coherence times as well.

ACKNOWLEDGMENTS. We acknowledge R. Hanson, G. de Lange, M. Veldhorst, S. Bartlett, and L. Schreiber for useful discussions, and R. Schouten and R. Vermeulen for technical support. This work was supported in part by Army Research Office (W911NF-12-0607), the Dutch Foundation for Fundamental Research on Matter (FOM), and a European Research Council (ERC) Synergy grant; development and maintenance of the growth facilities used for fabricating samples is supported by Department of Energy (DOE) (DE-FG02-03ER46028). E.K. was supported by a fellowship from the Nakajima Foundation. This research used National Science Foundation-supported shared facilities at the University of Wisconsin-Madison. Work at the Ames Laboratory (analysis of nuclear spin noise and decoherence) was supported by the DOE-Basic Energy Sciences under Contract DE-AC02-07CH11358.

1. Fowler AG, Mariantoni M, Martinis JM, Cleland AN (2012) Surface codes: Towards practical large-scale quantum computation. *Phys Rev A* 86(3):032324.
2. Zwanenburg FA, et al. (2013) Silicon quantum electronics. *Rev Mod Phys* 85(3):961–1019.
3. Veldhorst M, et al. (2014) An addressable quantum dot qubit with fault-tolerant control-fidelity. *Nat Nanotechnol* 9(12):981–985.
4. Veldhorst M, et al. (2015) A two-qubit logic gate in silicon. *Nature* 526(7573):410–414.
5. Muhonen JT, et al. (2014) Storing quantum information for 30 seconds in a nanoelectronic device. *Nat Nanotechnol* 9(12):986–991.
6. Kim D, et al. (2014) Quantum control and process tomography of a semiconductor quantum dot hybrid qubit. *Nature* 511(7507):70–74.
7. Kawakami E, et al. (2014) Electrical control of a long-lived spin qubit in a Si/SiGe quantum dot. *Nat Nanotechnol* 9(9):666–670.
8. Maune BM, et al. (2012) Coherent singlet-triplet oscillations in a silicon-based double quantum dot. *Nature* 481(7381):344–347.
9. Tyryshkin AM, et al. (2011) Electron spin coherence exceeding seconds in high-purity silicon. *Nat Mater* 11(2):143–147.
10. Morton JJL, McCamey DR, Eriksson MA, Lyon SA (2011) Embracing the quantum limit in silicon computing. *Nature* 479(7373):345–353.
11. Elzerman JM, et al. (2004) Single-shot read-out of an individual electron spin in a quantum dot. *Nature* 430(6998):431–435.
12. Scarlino P, et al. (2014) Spin-relaxation anisotropy in a GaAs quantum dot. *Phys Rev Lett* 113(25):256802.
13. Maudsley A (1986) Modified Carr-Purcell-Meiboom-Gill sequence for NMR Fourier imaging applications. *J Magn Reson* 69(3):488–491.
14. Álvarez GA, Souza AM, Suter D (2012) Iterative rotation scheme for robust dynamical decoupling. *Phys Rev A* 85(5):052324.
15. Gullion T, Baker DB, Conradi MS (1990) New, compensated Carr-Purcell sequences. *J Magn Reson* 89(3):479–484.
16. de Lange G, Wang ZH, Ristè D, Dobrovitski VV, Hanson R (2010) Universal dynamical decoupling of a single solid-state spin from a spin bath. *Science* 330(6000):60–63.
17. Carr H, Purcell E (1954) Effects of diffusion on free precession in nuclear magnetic resonance experiments. *Phys Rev* 94(3):630–638.
18. Meiboom S, Gill D (1958) Modified spin-echo method for measuring nuclear relaxation times. *Rev Sci Instrum* 29(8):688–691.
19. Souza AM, Álvarez GA, Suter D (2012) Effects of time-reversal symmetry in dynamical decoupling. *Phys Rev A* 85(3):032306.
20. Wang ZH, et al. (2012) Effect of pulse error accumulation on dynamical decoupling of the electron spins of phosphorus donors in silicon. *Phys Rev B* 85(8):085206.
21. Bluhm H, et al. (2010) Dephasing time of GaAs electron-spin qubits coupled to a nuclear bath exceeding 200 μs. *Nat Phys* 7(2):109–113.
22. de Sousa R (2009) Electron spin as a spectrometer of nuclear-spin noise and other fluctuations. *Electron Spin Resonance and Related Phenomena in Low-Dimensional Structures*, ed Fanciulli M (Springer, Heidelberg), pp 183–220.
23. Uhrig GS (2007) Keeping a quantum bit alive by optimized π-pulse sequences. *Phys Rev Lett* 98(10):100504.
24. Cywinski L, Lutchyn RM, Nave CP, Das Sarma S (2008) How to enhance dephasing time in superconducting qubits. *Phys Rev B* 77(17):174509.
25. Medford J, et al. (2012) Scaling of dynamical decoupling for spin qubits. *Phys Rev Lett* 108(8):086802.
26. Bylander J, et al. (2011) Noise spectroscopy through dynamical decoupling with a superconducting flux qubit. *Nat Phys* 7(7):565–570.
27. Cywiński L, Witzel WM, Das Sarma S (2009) Electron spin dephasing due to hyperfine interactions with a nuclear spin bath. *Phys Rev Lett* 102(5):057601.
28. Yang W, Liu RB (2009) Quantum many-body theory of qubit decoherence in a finite-size spin bath. II. Ensemble dynamics. *Phys Rev B* 79(11):115320.
29. Bergli J, Galperin YM, Altshuler BL (2009) Decoherence in qubits due to low-frequency noise. *New J Phys* 11(2):025002.
30. Knill E, et al. (2008) Randomized benchmarking of quantum gates. *Phys Rev A* 77(1):012307.
31. Magesan E, Gambetta JM, Emerson J (2012) Characterizing quantum gates via randomized benchmarking. *Phys Rev A* 85(4):042311.
32. Barends R, et al. (2014) Superconducting quantum circuits at the surface code threshold for fault tolerance. *Nature* 508(7497):500–503.
33. Muhonen JT, et al. (2015) Quantifying the quantum gate fidelity of single-atom spin qubits in silicon by randomized benchmarking. *J Phys Condens Matter* 27(15):154205.
34. Chuang IL, Nielsen MA (1997) Prescription for experimental determination of the dynamics of a quantum black box. *J Mod Opt* 44(11-12):2455–2467.
35. Kim D, et al. (2015) High-fidelity resonant gating of a silicon-based quantum dot hybrid qubit. *npj Quantum Inf* 1:15004.
36. Fogarty MA, et al. (2015) Nonexponential fidelity decay in randomized benchmarking with low-frequency noise. *Phys Rev A* 92(2):022326.
37. Epstein JM, Cross AW, Magesan E, Gambetta JM (2014) Investigating the limits of randomized benchmarking protocols. *Phys Rev A* 89(6):062321.
38. Vandersypen LMK, Chuang IL (2005) NMR techniques for quantum control and computation. *Rev Mod Phys* 76(4):1037–1069.
39. Shulman MD, et al. (2012) Demonstration of entanglement of electrostatically coupled singlet-triplet qubits. *Science* 336(6078):202–205.
40. Baart TA, et al. (2016) Single-spin CCD. *Nat Nanotechnol* 11(4):330–334.